RSC Advances

PAPER

View Article Online
View Journal | View Issue

Cite this: *RSC Adv.*, 2015, **5**, 20747

Austenitic stainless steel strengthened by the *in situ* formation of oxide nanoinclusions

Kamran Saeidi,[a] Lenka Kvetková,[b] František Lofaj[c] and Zhijian Shen*[a]

Received 19th December 2014
Accepted 12th February 2015

DOI: 10.1039/c4ra16721j

www.rsc.org/advances

An austenitic stainless steel was prepared by laser melting. High resolution transmission electron microscopy with energy dispersive spectrometry confirmed the *in situ* formation of oxide nanoinclusions with average size less than 50 nm. Scanning electron microscopy examination revealed the homogeneous dispersion of the oxide nanoinclusions in the steel matrix. The tensile and yield strengths of the prepared specimens were 703 and 456 MPa respectively with high ductility which is significantly improved compared to its conventionally casted counterpart.

Introduction

Adding nano-sized oxide particles inside a steel matrix significantly improves materials properties demanded for high temperature applications.[1–5] The oxide particles are very stable at temperatures close to the melting point of the steel and can effectively increase the high temperature strength of the steel. Fine dispersion of oxide particles can also increase the irradiation resistance of stainless steel grades such as 304 and ferritic steels.[6–9]

Powder metallurgy approaches, *e.g.* mechanical alloying (MA) followed by sintering such as hot isostatic pressing (HIP), are by far the predominant methods for preparing oxide dispersed steels (ODS).[10–14] Compared to the other preparation methods, MA has some distinctive advantages.[10] Although this method is indeed effective for formation of ODS, homogeneous distribution of nanoparticles is very difficult to achieve. Moreover, contaminants can easily be introduced during MA process, which has negative consequences. For instance, Xu *et al.* reported that impurity elements introduced during MA reduces ductility of ODS 304 to great extent.[15]

Laser sintering or laser melting (LS/LM) is a novel material processing method which belongs to a family of technologies known as additive manufacturing or even more commonly as 3D printing. During this process of melting the powder granules droplet by droplet in an inert atmosphere, normally it is conducted in argon or nitrogen, oxidation of the newly formed melts is almost an unavoidable problem. This is due to the presence of oxide impurities in the powder and the presence of a partial pressure of oxygen in the building chamber. This possible oxidation has usually been regarded as an obvious disadvantage, but it may turn to be an advantage when it can be manipulated in a controlled manner as it is reported in this article. When the oxygen inside the LS/LM chamber is consumed by the formation of nanoparticle of certain oxides, the risk of contamination of the steel would be significantly reduced. The *in situ* formed oxide nanoparticle may gain a degree of homogenous distribution that can hardly be achieved by the conventional powder metallurgy approaches.[16–21]

The aim of the present work is to report a new approach for forming ODS austenitic 316L steel by controlled oxidation during LM process. The chemical composition, phase constitutions and their distribution of *in situ* formed oxide nanoparticles inside the steel matrix were characterized by means of electron microscopy (SEM/TEM/EDS) observations. The mechanical properties of the obtained ODS materials were characterized and compared with the conventionally casted 316L steel and ODS 304 austenitic steel prepared by powder metallurgy approach.

Experimental

Laser melted specimens with the dimension of 40 × 4 × 1 mm were prepared from 316L stainless steel powder. Two different hatching distances of 40 mm and 4 mm were applied, hereafter referred as S1 and S2 strategies. The specimens prepared under these two scanning strategies were labeled as S1 and S2 accordingly. Laser melting was performed in an EOSINT M 270 laser sintering system with fixed laser parameters. The sintering was performed in Ar atmosphere with residual oxygen inside the chamber of 0.1%. Microstructure characterizations were performed using scanning electron microscope (SEM, JEOL JSM-7000F, JEOL, Tokyo, Japan). Verifying the dispersion of oxide nanoparticles was carried out by transmission electron microscopes (TEM, FEG-2100F and LaB6 2100 JEOL, Tokyo,

[a]*Department of Materials and Environmental Chemistry, Arrhenius Laboratory, Stockholm University, S-106 91 Stockholm, Sweden. E-mail: shen@mmk.su.se; Fax: +46 8 152187; Tel: +46 8 162388*

[b]*Institute of Materials Research of the Slovak Academy of Sciences, Watsonova 47, Kosice, Slovakia*

[c]*Faculty of Materials Science and Technology in Trnava, Slovak University of Technology in Bratislava, 916 24 Trnava, Slovak Republic*

Japan). TEM specimens were prepared by Jet-polishing (TenuPol-5, Struers, Ballerup, Denmark).

Tensile specimens were cut by electrical discharge machine (EDM) and then machined into dog-bone shape specimens. Five tensile specimens were used to assure sufficient statistical reliability. The tensile strength and yield stress were measured using standard testing machine TIRAtest 2300 (Schalkau, Germany) with the pneumatic grips and the cross head speed of 0.5 mm min^{-1}. The values for the mechanical data is an average obtained from all five specimens. Conventional microhardness has been measured using Leco LM700AT, (Leco Corporation, USA) with the Vickers indenter at the load of 10 N. The instrumented nanohardness was measured using Berkovich indenter on TTX-NHT nanoindenter (CSM Instruments, Switzerland) in single loading–unloading mode up to 100 mN at the loading–unloading rate of 100 mN min^{-1}. Mechanical properties measurements were conducted on laser melted samples with S1 and S2 strategies.

Results and discussion

A back scattered SEM micrograph taken on argon ion polished surface of a specimen prepared under a chamber oxygen content of 0.1% is shown in Fig. 1a. Besides the large grains of austenite visible due to their orientation contrast, a number of black spherical inclusions can be seen. The inclusions are very fine and nano sized with average diameter of 50 nm, well dispersed inside the steel matrix. The amount of the nanoinclusions obtained by image analysis was approximately 6 vol%.

Fig. 1b shows the high resolution transmission electron microscopy (HRTEM) taken around a spherical inclusion. The inset (i) is a EDP taken in the middle of the spherical inclusion which shows a complete amorphous structure and inset (ii) is an EDP taken from the boundary area between the spherical inclusion and its neighboring crystalline grain. As seen, the spherical inclusion is amorphous and the neighboring sites is crystalline. The crystallinity of the neighboring site can be clearly identified with clear lattice fringes.

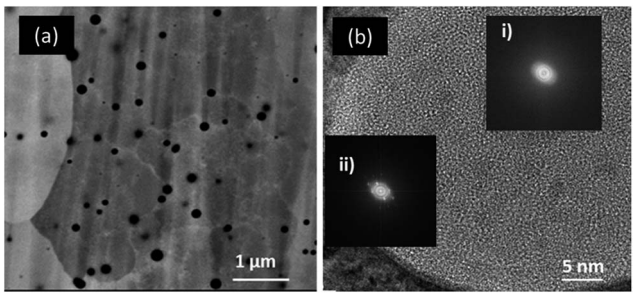

Fig. 1 A back scattered SEM micrograph taken on argon ion polished surface (a) and a HRTEM micrograph taken around a nanoinclusion (b). The former reveals the formation of well dispersed spherical nanosized inclusions with dark contrast, while the later confirms the complete amorphous nature of the spherical inclusion.

TEM elemental mapping taken from an area containing the nanoinclusions shown in Fig. 2 indicates that the nanoinclusions contain mostly Si and O. The almost ideal spherical shape of the inclusion and sharp interface between inclusion and steel matrix support the suggestion that the inclusion was originally in a melt state. Sharp interface would result from poor wettability due to high surface tension and subsequently extremely low solubility of oxide phase in steel even at high temperatures achieved under the laser beam. Formation of these circular nanoinclusions can be explained well thermodynamically. As, Si has much higher oxygen affinity compared to other alloying elements inside the 316L steel composition. According to Elingham diagram for oxides[22] the standard Gibbs free energy changes for SiO_2 is more negative than that for oxides of Cr, Mo, Ni, and Fe at all temperatures. For example, the calculated equilibrium partial pressure of oxygen for Si at 1673 K is about 2.4×10^{-20} atmosphere and for Ni is about 9.5×10^{-5}. It means at 1673 K and any oxygen partial pressure higher than 2.4×10^{-20} atmosphere Si can oxidize readily. This implies that Si will preferentially react with oxygen presented inside the steel powder or in the laser chamber.

Tensile curves for all sets of specimens are shown in Fig. 3a. The as laser melted specimen S2 has a higher tensile and yield strength with 703 ± 8 MPa and 456 ± 17 MPa, respectively, compared to that of the specimen S1, being 654 ± 49 MPa and 428 ± 35 MPa, respectively. However, it should be noted that the values of yield strength (YS) and tensile strength (TS) are average of 5 identical samples and individually the mechanical properties of S2 was higher than S1. Although the tensile properties of the two specimens are different, both specimens show very similar ductility, being 45% and 46% elongation, respectively. The difference in tensile properties for two types of specimens is due to the hatching distance applied that determines the exposure overlap. *i.e.* Specimen S1 is prepared with a hatching distance of 40 mm by which the laser scans a longer focusing path which would result in lower intensity and less effective

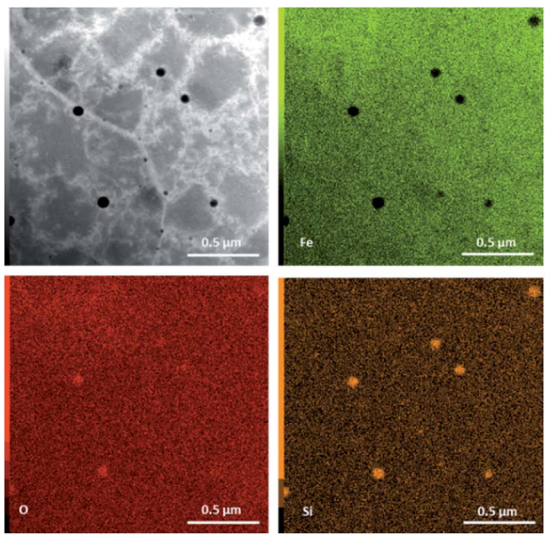

Fig. 2 TEM elemental mapping taken from an area containing the nanoinclusions. The nanoinclusions contain mostly Si and O.

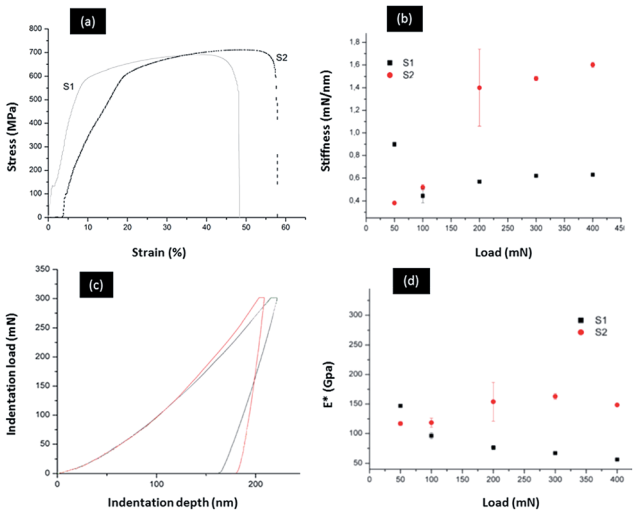

Fig. 3 Tensile curve (a), (b), stiffness of the specimens (c) instrumented nano indentation curve and reduced elastic modulus plot (d).

melting compared to specimen S2 with hatching distance of 4 mm. Therefore specimen S2 is more effectively melted and has higher mechanical properties than specimen S1.

Table 1 summarizes the results of the measured mechanical properties in comparison with some reference data. As seen, all mechanical properties of ODS LM (S1 and S2) specimens are superior to that of conventional cast 316L.

The higher hardness and tensile strength of ODS specimens are due to dispersion of oxide particles that act as effective barriers against dislocation motion during tensile deformation.[23,24] Compared with MA-HIP ODS 304 the ODS LM specimens show higher yield strength and much higher ductility. More homogenous dispersion of oxide nanoinclusions and no contamination involved in ODS LM are believed to be the reasons behind this improvement. Yield strength (YS) and hardness for metals and alloys are mechanical properties that are related to the resistance of materials to deformation. The relation between YS and hardness is well established in literature.[25,26] In ODS LM samples (S1 and S2) the well dispersed spherical oxide nanoinclusions in the steel matrix together with the nature of laser melted steel[27] that has a high dislocation density and fine grains, result in higher YS and hardness compared to conventionally cast steel.

The instrumented nano indentation curve is shown in Fig. 3b. The two set of specimens represent the same plastic deformation behavior but specimen with S2 strategy being slightly harder. Values for the nanoindentation and conventional indentation measurements under the load of 100 mN and 10 N respectively are also shown in Table 1. The difference in hardness values can be related to two overlapping effects related to the indent size; which are conventional indentation size effect (ISE) and the effect of the size of the nanoinclusions.

When the indentation is carried out at low loads where the indentation size is small, effect of secondary phases or precipitates inside the material matrix can also be studied.[28,29] Nevertheless, the values obtained with a nanoindenter tip and so low loads can still be overstated due to small size effect (ISE) of the indenter, which contains smaller area of sample which could possibly be rich in nanoinclusions, *i.e.* the indent size may be comparable with the size of the oxide inclusions. Because silica is substantially harder (~900 HV) than the hardness range in steels (178–458 HV), the contribution of hard inclusions to the resulting hardness is in the case of small (loads) indents which is much higher than that in the large (loads) indents; when the effect of inclusions is averaged over larger area of softer matrix. Therefore to make more accurate and acceptable measurement a micro-indenter tip and microhardness measurements were also carried out, this represents hardness of the overall material without taking into account only the effect of harder nanoinclusions. Thus, the hardness values of 315 HV and 325 HV obtained at 10 N load for specimens with S1 and S2 strategy respectively is considered to be the representative macro-hardness of the studied ODS steel of the material. However the studied LM ODS steel is substantially harder than the conventionally made 316L steel.[30]

Stiffness of the specimens was worked out from the curves shown in Fig. 3b using eqn (1) and the results are shown in Fig. 3c.

$$S = \frac{F_{\max}}{h_e} = \frac{dF}{dh} \quad (1)$$

where S is stiffness and h_e is point of the tangent to curve at $F_{\max}$ with the indentation depth axis (elastic depth). At higher loads specimen S2 has higher stiffness.

The reduced elastic modulus of the specimens were calculated from the curve shown in Fig. 3b and by using eqn (2). The results are shown in Fig. 3d.

$$E^* = \frac{dF}{2dh}\frac{\sqrt{\pi}}{A_p} \quad (2)$$

where E^* is the reduced elastic modulus and A_p is projected contact area of the indentation at the contact depth of h. Projected contact area has been calibrated using standard

Table 1 Summary of the measured mechanical properties in comparison with the reference data

Sample	As LM S1	As LM S2	Cast 316L[30]	MA-HIP ODS 304 (ref. 15)
Microhardness (HV)	325 ± 5	315 ± 5	227	—
Nano hardness (HV)	400 ± 6.6	437 ± 48	—	—
YS (MPa)	428 ± 35	456 ± 17	310	300
TS (MPa)	654 ± 49	703 ± 8	620	775
Elongation (%)	45 ± 6	46 ± 7	30	20–25
Density (g cm^{-3})	7.84	7.79	—	—

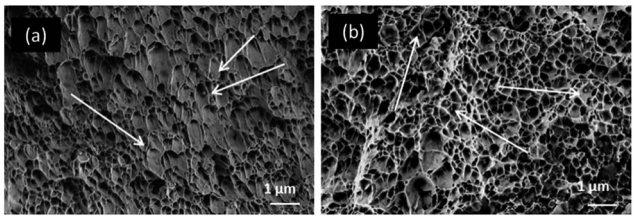

Fig. 4 Fracture surface of laser melted specimens with (a) S1 and (b) S2 strategies. The oxide particles are seen inside the dimples pointed out by white arrows.

procedure on fused silica to eliminate the effect of indenter curvature, which is especially important at small penetration depths. Again at medium to high loads specimen S2 has much higher elastic modulus. As mentioned before, in specimen S2 with shorter hatching distance, laser beam has strong overlap and the material is exposed to laser more effectively.

The fracture surface of the as laser melted specimens is shown in Fig. 4. Both S1 and S2 specimens have similar fracture surface. It clearly shows the presence of multi scale micron and nano dimples throughout the entire fracture surface indicating ductile fracture mode. The oxide nanoparticles are uniformly dispersed through the dimples as pointed out by the white arrows. The size, distance between oxides and the deformability of the oxides play a significant role in strengthening the steel matrix.

Conclusions

In summary 316L austenitic steel was prepared by laser melting of powder granules in argon atmosphere with controlled oxygen partial pressure. It was found that oxide particles around 50 nm formed and were finely dispersed inside the steel matrix. The *in situ* formed oxide nanoinclusions are amorphous and contained Si and O as well as small amount of Cr. At room temperature the ODS LM 316L steel achieved a tensile strength and a yield strength of 703 MPa and 456 MPa, respectively, which are higher compared to that of the conventionally casted 316L steel. Multi scale dimples and very fine oxide nanoinclusions well dispersed in the steel matrix along with no contamination of the steel rendered a high ductility with 46% elongation for the ODS LM 316L steel, which is much higher compared to that of ODS 304 steel prepared by HIPing of mechanically alloyed powder.

Acknowledgements

This work was supported by grants from the Swedish Research Council (VR) and VEGA project 2/0098/14. The microstructural characterization part of the work was performed at the Electron Microscopy Centre of Stockholm University. The authors would acknowledge K. Jansson and X. Gao for their supports on the electron microscopy works, F. Linberg for TEM specimen preparation and T. Ekström for fruitful comments on the manuscript.

Notes and references

1 K. L. Murty and I. Charit, *J. Nucl. Mater.*, 2008, **383**, 189.
2 A. F. Rowcli, *J. Nucl. Mater.*, 2008, **263**, 183.
3 N. Akasaka, S. Yamashita, T. Yoshitake, S. Ukai and A. Kimura, *J. Nucl. Mater.*, 2004, **329**, 1053.
4 D. T. Llewellyn, *Steels: metallurgy and applications*, Butterworth–Heinemann, Oxford, 1992.
5 T. K. Kim, C. S. Bae, D. H. Kim, J. S. Jang, S. H. Kim, C. B. Lee and D. H. Hahn, *Nucl. Eng. Technol.*, 2008, **40**, 305.
6 A. Ramar, N. Baluc and R. Schäublin, *J. Nucl. Mater.*, 2007, **367**, 217.
7 M. K. Miller, D. T. Hoelzer, E. A. Kenik and K. F. Russell, *Intermetallics*, 2005, **13**, 387.
8 C. Suryanarayana, *Prog. Mater. Sci.*, 2001, **46**, 1.
9 S. Ukai and M. Fujiwara, *J. Nucl. Mater.*, 2002, **307**, 749.
10 C. Suryanarayana, E. Ivanov and V. V. Boldyrev, *Mater. Sci. Eng., A*, 2001, **304**, 151.
11 M. Fujiwara, S. Ukai, M. Harada, H. Okada, M. Inoue, S. Nomura, S. Shikakura, K. Asabe and T. Nishida, *J. Nucl. Mater.*, 1993, **204**, 65.
12 K. Asabe, S. Ukai, M. Harada, H. Okada, M. Inoue, S. Nomura, S. Shikakura, T. Nishida and M. Fujiwara, *J. Nucl. Mater.*, 1993, **204**, 74.
13 S. Ukai, T. Nishida, H. Okada, T. Okuda, M. Fujiwara and K. Asabe, *J. Nucl. Sci. Technol.*, 1997, **34**, 256.
14 M. B. Toloczko, D. S. Gelles, F. A. Garner, R. J. Kurtz and K. Abe, *J. Nucl. Mater.*, 2004, **329**, 352.
15 Y. Xu, Z. Zhou, M. Li and P. He, *J. Nucl. Mater.*, 2011, **417**, 283.
16 M. Wang, Z. Zhou, H. Sun, H. Hu and S. Li, *J. Nucl. Mater.*, 2012, **430**, 259.
17 M. Wang, Z. Zhoun, H. Sun, H. Hu and S. Li, *J. Mater. Sci. Eng. A*, 2013, **559**, 287.
18 M. P. Phaniraj, D. I. Kim, J. H. Shim and Y. W. Cho, *Acta Mater.*, 2009, **57**, 1856.
19 Q. X. Sun, Y. Zhou, Q. F. Fang, R. Gao, T. Zhang and X. P. Wang, *J. Alloys Compd.*, 2014, **598**, 243.
20 S. Noha, A. Kimurab and T. K. Kim, *Fusion Eng. Des.*, 2014, **89**, 1746.
21 V. V. Sagaradze, V. I. Shalaev, V. L. Arbuzov, B. N. Goshchitskii, Y. Tian, W. Qun and S. Jiguang, *J. Nucl. Mater.*, 2001, **295**, 265.
22 D. Gaskell, *Introduction to the thermodynamics of materials*, Taylor &Francis, 5th edn, 2008.
23 E. Gaganidze and J. Aktaa, *Fusion Eng. Des.*, 2013, **88**, 118.
24 S. Ohtsuka, S. Ukai, H. Sakasegawa, M. Fujiwara, T. Kaito and T. Narita, *et al.*, *J. Nucl. Mater.*, 2007, **367**, 160.
25 O. Takakuwa, Y. Kawaragi and H. Soyama, *J. Surf. Eng. Mater. Adv. Technol.*, 2013, **3**, 262.
26 J. T. Busby, M. C. Hash and G. S. Was, *J. Nucl. Mater.*, 2005, **336**, 267.
27 K. Saeidi, X. Gao, Y. Zhong and J. Shen, *J. Mater. Sci. Eng. A*, 2015, **625**, 221.
28 M. Masanta, S. M. Shariff and A. R. Choudhury, *J. Mater. Sci. Eng. A*, 2011, **528**, 5327.
29 T. Kavetskyy, J. Borc, K. Sangwal and V. Tsmots, *J. Optoelectron. Adv. Mater.*, 2010, **12**, 2082.
30 A. D. Romig Jr, *ASM Handbook Properties and Selection: Irons, Steels, and High-Performance Alloys*, ASM international, 1990, vol. 1.

